Ferromagnetic resonance in a topographically modulated permalloy film

J. Sklenar,[1] P. Tucciarone,[2] R. J. Lee,[1] D. Tice,[3] R. P. H. Chang,[4] S. J. Lee,[5] I. P. Nevirkovets,[1]
O. Heinonen,[6,1] and J. B. Ketterson[1,7]

[1]*Department of Physics and Astronomy, Northwestern University, Evanston, Illinois 60208, USA*
[2]*Department of Chemical and Biological Engineering, University at Buffalo (SUNY), Buffalo, New York 14260, USA*
[3]*Department of Chemistry, Northwestern University, Evanston, Illinois 60208, USA*
[4]*Department of Materials Science and Engineering, Northwestern University, Evanston, Illinois 60208, USA*
[5]*Department of Physics, Hanyang University, Seoul 133-791, South Korea*
[6]*Materials Science Division, Argonne National Laboratory Argonne, Illinois 60439, USA*
[7]*Department of Electrical and Computer Engineering, Northwestern University, Evanston, Illinois 60515, USA*

(Received 7 August 2014; revised manuscript received 17 March 2015; published 23 April 2015)

A major focus within the field of magnonics involves the manipulation and control of spin-wave modes. This is usually done by patterning continuous soft magnetic films. Here, we report on work in which we use topographic modifications of a continuous magnetic thin film, rather than lithographic patterning techniques, to modify the ferromagnetic resonance spectrum. To demonstrate this technique we have performed in-plane, broadband, ferromagnetic resonance studies on a 100-nm-thick permalloy film sputtered onto a colloidal crystal with individual sphere diameters of 200 nm. Effects resulting from the, ideally, sixfold-symmetric underlying colloidal crystal were studied as a function of the in-plane field angle through experiment and micromagnetic modeling. Experimentally, we find two primary modes; the ratio of the intensities of these two modes exhibits a sixfold dependence. Detailed micromagnetic modeling shows that both modes are quasiuniform and nodeless in the unit cell but that they reside in different demagnetized regions of the unit cell. Our results demonstrate that topographic modification of magnetic thin films opens additional directions for manipulating ferromagnetic resonant excitations.

DOI: 10.1103/PhysRevB.91.134424 PACS number(s): 76.50.+g, 75.30.Ds, 75.75.−c, 75.78.Cd

The phenomenon of ferromagnetic resonance (FMR) has been widely used to study the dynamic properties of magnetic nanostructures. The fabrication technique most commonly used is lithography, which can be expensive and is limited by the available lithographic resolution; furthermore, producing topography introduces additional difficulties, even though some very intricate and complex structures—with very complex dynamics—have been produced [1]. Nevertheless, tailoring of magnetic films through lithographic means has revealed a host of interesting effects associated with the dynamic properties of these structures. In periodically patterned continuous structures, spin-wave control is realizable and has been paramount in the field of magnonics; this has been recently reviewed [2]. In contrast, isolated structures, like disks, harbor unique magnetic modes from single magnetic domain confinement [3]. An example of a confined mode is a vortex mode within an individual magnetic disk. The excitation of associated vortex modes has been exploited to change the vortex state of the disk [4]. More recently, FMR has been proposed as a tool to study geometric frustration in periodically patterned artificial spin-ice structures [5]. The varying scope in these works is owed to the fact that much of the physics arises from geometrical demagnetization defined by the sample fabrication.

In this work we have studied how topography can modify the FMR spectrum of a permalloy (Py) film deposited on a colloidal crystal. To create this sample we have sputtered a Py film directly on top of a colloidal crystal, a self-assembled hexagonal close packed (hcp) array of polystyrene spheres. Compared to lithographically defined samples, far less work has been done using this approach. The geometrical details of these structures are not easily reproduced through lithography and, depending on the colloid diameter, small distance scales are readily achievable. Thus far the magneto-optical properties of magnetic films on colloidal crystals have been investigated [6]. Following this initial work there has been interest in geometrical frustration being built into such nanostructures [7–9]. In those works the frustration originated from the remanent state vortex on a given dome being unable to satisfy all its nearest-neighbor interactions with other vortices within the hcp lattice. In lithographically defined samples there is a precedent for investigating, via FMR, structures that support vortices as they are a hotbed for new modes of excitation. Yet for our topographically modified system there appears to be no ferromagnetic resonance study. There has been a FMR study on Co/Pt/FeMn multilayers grown on top of a colloidal crystal [10]. In that work, colloidal crystals provide a curved substrate that can allow for additional tunability of magnetic anisotropy in magnetic multilayer systems [11,12]. We do note that FMR studies have been performed on inverse-opal structures that utilize colloidal crystals as a template of sorts [13].

The colloidal crystals serving as templates for our magnetic films are made from 200-nm-diameter polystyrene spheres. Synthesis was accomplished using the well-known vertical deposition method [14]. Here, the lower part of a glass slide is immersed in a vial containing a solution of spheres in deionized water. The vial is placed within an oven and the water is allowed to evaporate. Crystal growth occurs at the evaporation line where the water meniscus contacts the glass slide. Our samples are single crystals over approximately a 1×1 cm^2 area. The colloidal crystal orientation has been verified to be preserved across this entire area by imaging different regions

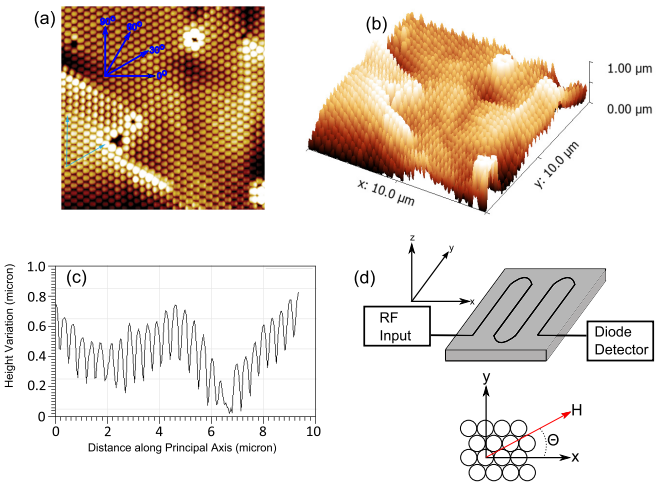

FIG. 1. (Color online) (a) is an AFM image of the colloidal crystal after Py sputtering; (b) shows the topographical uniformity of the resulting structure and commonly observed crystal defects; (c) is the height variation of the structure along one of the lattice vectors. The gray slab in the top inset of (d) is a representation of the sample. The black winding wire indicates the meanderline through which *rf* passes; the turn spacing is close to 2 mm. The meanderline and sample lie in the *XY* plane and the field angle is measured off the x axis. The (100) crystal lattice direction lies along the x axis.

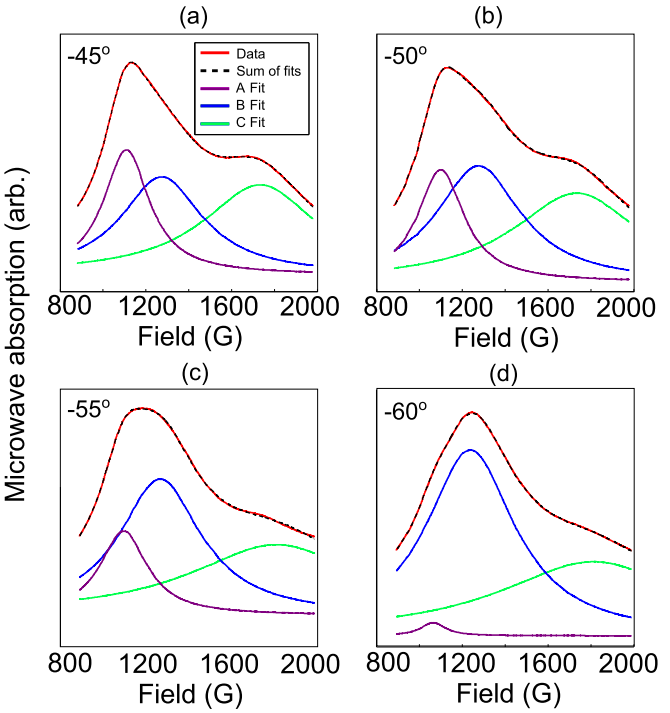

FIG. 2. (Color online) (a)–(d) show the integrated FMR spectra at $-45°$, $-50°$, $-55°$, and $-60°$ each as a red line. The pink, blue, and green curves are the fitted contributions of the ***A***, ***B***, and ***C*** peaks. The sum of the fits, which is essentially indistinguishable from the data, is denoted as a dashed black line. Notice how the amplitude of the ***B*** peak rises relative to the ***A*** peak at $-60°$.

across the sample to check for rotations of the lattice vectors. After the crystals are fabricated, 40 nm of Ag followed by 100 nm of Py is sputtered onto the sample. The resulting structure can be seen in Fig. 1. In Fig. 1(a) a top-down atomic force microscope (AFM) image clearly shows the hcp structure and sixfold symmetry. Some crystal defects, vacancies, and line defects are also seen. Additionally, the absolute height can change because the number of stacked spheres beneath the Py film can vary. An AFM-extracted topographical map (of the same region) is shown in Fig. 1(b); Fig. 1(c) shows a one-dimensional cut with the height variation along a lattice vector.

To excite ferromagnetic resonance over a large area of the sample we utilize a meander line technique [15]. Here we press a serpentine Cu wire over the surface of the Py film as shown in Fig. 1(d). The microwaves pass through the meander line and a ground plane lies beneath the sample. The output signal from the meander line is rectified by a microwave diode and sent to a lock-in amplifier. During experiments we fix an excitation frequency of 10 GHz at 10 dBm (not including line losses) and sweep the magnetic field looking for microwave absorption as we modulate the magnetic field with a 40 Hz, 20 G rms, ac magnetic field. For the experiments presented here we keep the magnetic field in the plane of the sample and rotate the in-plane field angle. The in-plane field angle with reference to the colloidal crystal crystalline axes is shown in Fig. 1(d). When the in-plane field angle is $0°$ we expect the meander line to have the weakest coupling to FMR because a significant portion of the exciting field will be parallel to the applied field. At this angle we expect the sample area that is near the turns of the meander line to be excited. By the same argument, when the in-plane angle is $\pm 90°$ we expect the greatest coupling to FMR because a larger area of the sample is excited. Because the sample's physical properties and geometry are uniform over an area much larger than the footprint of the meander line, we do not expect the meander line to excite different types of modes if the orientation relative to the sample is changed; only the surface area excited should change. Additionally, the microwave field generated by the meander line is periodic on a 1 mm length scale, which is much longer than the colloidal crystal periodicity. Therefore, we expect to excite modes with a wave vector near $k = 0$. As the periodic topography of our system will endow magnetization dynamics with a spin-wave band strucure, any modes that we excite should be $k = 0$ modes at the Γ point in the first Brillouin zone.

Figure 2 depicts integrated spectra obtained experimentally at a microwave frequency of 10 GHz. We resolve three distinct modes centered around 1050, 1200, and 1750 G that we respectively name ***A***, ***B***, and ***C***. For a uniform film the resonance field would be expected to lie just below 1100 G. This suggests that the modes are modifications of the uniform precession mode (the Kittel mode) caused by topography-induced demagnetization. We also rotate the in-plane field angle to study the influence of the underlying sixfold symmetry. Some examples of FMR spectra for in-plane field angles between $-45°$ and $-60°$ that represent those observed are shown in Figs. 2(a)–2(d). The ***A***, ***B***, and ***C*** modes are extracted by fitting the spectra to a superposition of Lorentzian functions. We will focus our current discussion on the ***A*** and ***B*** modes. The field positions of these modes over a $180°$ range are shown in Fig. 3(a) as blue circles.

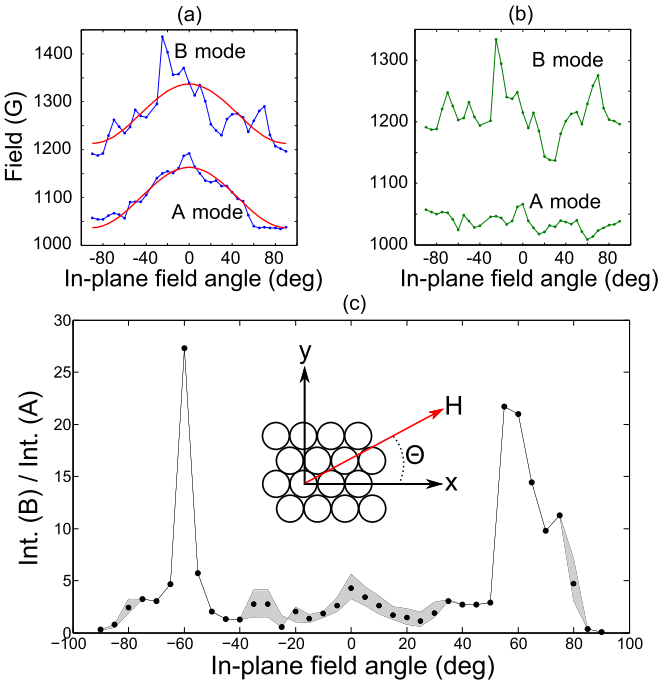

FIG. 3. (Color online) (a) shows the field dependence of both the ***A*** and ***B*** modes extracted from fitting. Aside from both branches being independent of one another there is an artificial twofold angular dependence shown as the red line that is thought to arise from anisotropic sphere shrinkage. The remaining dependence after the anistropic part is removed is shown in (b). The sixfold-dependent ratio of the ***B*** peak intensity to the ***A*** peak intensity is shown in (c).

The individual branches are clearly independent from one another but there is an observed twofold symmetry in the field angles. We believe this twofold dependence to be artificially induced from shrinking that occurs in the spheres during drying following deposition. From scanning electron microscopy (SEM) results (see Supplemental Material [16]) an approximately 5% variation is measured in the diameter of the spheres. To remove this artificial effect we fit a $\cos^2(\theta)$ function to the field positions, shown as red solid lines in Fig. 3(a). Subtracting this from the field positions yields the result in Fig. 3(b). It is important to note that these two branches appear to be independent. In Fig. 3(c) we plot the ratio of the intensities of the ***A*** and ***B*** modes to illustrate a very strong effect that is seen in Fig. 2. The effect is a sixfold variation in the ratio of the intensity of ***B*** to the intensity of ***A*** with maxima in this ratio at -60°, 0°, and $+60^\circ$; the mechanism behind this observation, a suppression of the intensity of ***A***, is described in the simulation results. Note that the maximum of the ***B*** to ***A*** ratio at 0° is attenuated compared to the ratio at $\pm 60^\circ$; we believe this to be caused by the sphere asymmetry that attenuates the amplitudes of *both* the ***A*** and ***B*** modes at 0°. The origin of the ***C*** mode may be demagnetized regions at defect edges. The high field and broad linewidth of the resonance are suggestive of a rough "edgelike" boundary mode; this is further corroborated by the numerical simulations of defect-free systems where such a mode cannot easily be detected, although for some field angles there is a hint of a shoulder at about 8 GHz (in a field of 1000 G), which may indicate the existence of a mode localized to small regions in the unit cell. It should be mentioned that when fitting the spectra a constrained parameter search is used to avoid unphysical fitting situations. The error bands shown in Fig. 3(c) are based on varying the limits of the upper and lower field ranges where the ***A*** and ***B*** modes are allowed to exist. The intrinsic error on the data points for a given constraint range is smaller than the data points.

To understand the microscopic origin of these resonances we performed micromagnetic simulations [17]. The simulation space consists of a $400 \times 346.4\ \text{nm}^2$ area (XY plane) containing four unit cells of the underlying hcp polystyrene lattice. The total thickness of the simulated structure is 100 nm but with a topography approximating that of the Py film on the polystyrene colloidal crystal. The maximum height of the film at a given (x,y) coordinate is given by the height the Py film would have on top of the underlying spheres; in this way we create the topographically modified film having a centered hexagonal structure. The simulated $400 \times 346.4 \times 100\ \text{nm}^3$ space including the Py film is discretized into $5 \times 3.4641 \times 5\ \text{nm}^3$ tetragonal mesh with a magnetization director in each cell. Periodic boundary conditions were applied in the (x,y)-plane with 6×6 images included in the calculation of the magnetostatic fields. The static and dynamic magnetization is described by the Landau-Lifshitz-Gilbert (LLG) equation

$$\frac{d\hat{m}(\mathbf{r},t)}{dt} = -|\gamma_e|\hat{m}(\mathbf{r},t) \times \mathbf{H}_{\text{eff}}(\mathbf{r},t) - \frac{|\gamma_e|\alpha}{1+\alpha^2}\hat{m}(\mathbf{r},t) \times [\hat{m}(\mathbf{r},t) \times \mathbf{H}_{\text{eff}}(\mathbf{r},t)]\,. \quad (1)$$

Here, $\hat{m}(\mathbf{r},t)$ is a unit vector along the local magnetization direction, γ_e is the electron gyromagnetic ratio, here set to 2.95 GHz/kOe, and α is the dimensionless damping set to 0.1 for static equilibration and 0.01 for the dynamic time-integration. The effective field $\mathbf{H}_{\text{eff}}$ includes near-neighbor exchange (calculated using a six-point stencil in the parallelepiped lattice), the external field, and magnetostatic (demagnetizing) fields. An exchange coupling typical for Py of about 1.3 μergs/cm was used (the modes at or near the Γ point are rather insensitive to the exact value of the exchange coupling), and a zero-temperature saturation magnetization of 800 emu/cm^3. The system was first equilibrated with the larger damping for a given direction of the external field, using time steps of up to 2 ps. This equilibrium structure was then subjected to a uniform magnetic field for a duration of up to 0.5 ns after which the magnetization dynamics was integrated for 10 ns in time steps of 250 fs using a modified Bulirsch-Stoer algorithm with error checking and adjustable time step. The magnetostatic fields were calculated at each time step by multiplying the Fourier-transformed instantaneous magnetization with the (stored) Fourier-transformed demagnetizing tensor, and back-transforming to the space domain. We confirmed that our results were not dependent on the used mesh with a tetragonal symmety and that they obey a sixfold symmetry in the plane by performing similar numerical simulations with a $2.5 \times 1.73205 \times 5\ \text{nm}^3$ tetragonal mesh on a numerical unit cell containing two primitive unit cells of the system but with 7×7 periodic images for field angles of 15°, 25°, 30°, 40°, 50°, and 60°. In order to obtain results that can be directly compared to experimental spectra we average the entire magnetization of the nanostructure at each time

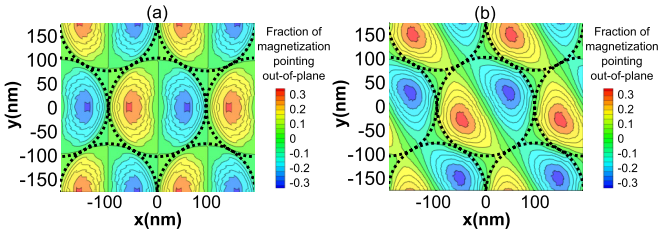

FIG. 4. (Color online) The simulated static configuration of magnetization is shown at 0° and 30° in (a) and (b) respectively. Specifically, we plot the fraction of the magnetization that is pointing out of plane. The largest tipping occurs where the magnetic field lines enter or exit an underlying colloid as indicated by the drawn-in arrows. Here 30% of the magnetization can tip out of the plane.

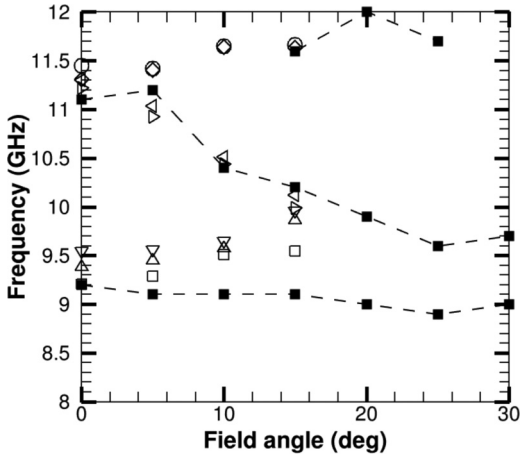

FIG. 5. Modeled resonant frequencies obtained through numerical diagonalization (empty symbols) and numerical integration and Fourier transform (filled squares and dashed lines). Only the range $0^\circ \leqslant \theta \leqslant 30^\circ$ is displayed as the frequencies are symmetric about $\theta = 30^\circ$.

step. This time sequence can then be Fourier transformed to obtain a spectrum for each component of the magnetization. Additionally, in order to obtain spatially resolved information of the modes, we also collect the magnetization at a given (x, y) coordinate for each time step to create a time sequence of two-dimensional (2D) magnetization maps. This sequence is then Fourier transformed with respect to time to obtain a spatial map of the magnetization amplitude and phase at each frequency [18].

We also performed direct numerical diagonalization of the linearized LLG equation at field angles from 0° to 30° in steps of 5°, and at 40°, 50°, and 60° using a numerical unit cell containing two primitive unit cells of the system, and with 7×7 periodic images and a tetragonal mesh of size $5 \times 3.4641 \times 5$ nm^3 and a damping of zero. This alternative way to obtain resonant modes of ferromagnetic microstructures and nanostructures has been well described and implemented before [19,20]. For smaller field angles, the agreement between the numerical diagonalization and the time integration is very good (we confirmed that the slightly lower frequencies obtained from the time integration are because of the finite damping; diagonalizing the linearized LLG equations with a finite damping of 0.01 pushed the frequencies down to the ones obtained by time integration). For larger field angles $\gtrsim$20°, the tetragonal lattice affects the numerical diagonalization and breaks the sixfold symmetry.

To illustrate the static configuration, we plot the out-of-plane fraction of the magnetization at 0° and 30° in-plane field directions in Fig. 4. The in-plane component of the magnetization largely follows the applied field direction so that the only variation in the static configuration is an out-of-plane tipping that follows the curvature of the underlying colloid. The out-of-plane tipping is greatest in regions where the field is normal to a vector that is tangent to the circular perimeter of an underlying colloid. Unsurprisingly, when the field is parallel to this type of vector there is little out-of-plane tipping.

The numerically obtained frequencies are shown as a function of field angle in Fig. 5, where the solid squares connected by dashed lines are the frequencies obtained from numerical time integration, and the open symbols (squares, triangles, circles, and diamonds) are from numerical diagonalization (these latter are displayed only for field angles $\theta \leqslant 15^\circ$ as the tetragonal lattice skewed the results for larger angles, as explained earlier). The numerical diagonalization yields a number of modes with odd symmetry in the unit cell along the field direction; these modes do not couple to the uniform field pulse. There is a band of three modes near 9.5 GHz which includes the Kittel-like nearly uniform mode that is excited by the uniform field pulse and obtained through numerical time integration at about 9 GHz. There is also a band of higher-order modes with frequencies between 10 and 11 GHz. One of the modes in this band has an even symmetry and couples to the uniform field pulse. Finally, there is a third band of modes close to 12 GHz, with a few of those coupling visibly to the uniform field pulse. The simulated spectra obtained through numerical time integration for field angles between 0° and 30° are shown in Fig. 6. It is clear that the higher-frequency peak couples very weakly to the uniform field pulse for field angles of 10° or smaller. The large peak found at all angles close to 9.0 GHz compares in field-frequency space to the experimentally observed ***B*** mode. We therefore identify the ***B*** mode as the Kittel-like near-uniform mode, and the higher-frequency band of modes as the ***A*** mode. We do not directly try to match the modes obtained from diagonalization with those obtained through time integration; for the remainder of our discussion we shall focus on the two primary modes ***A*** and ***B*** through the time-integration method.

To ascertain the topographical mode distributions of the ***A*** and ***B*** modes we plot amplitude and phase maps of each in Fig. 7 at an in-plane field angle of 30°. The lower-energy ***B*** mode has large precession in the more heavily demagnetized regions of the spheres that lie along stripes passing midway between lattice sites (between the spherical caps), as seen in Fig. 7(a). This region overlaps closely with that where the out-of-plane tipping of the static configuration is nearly 30%. The precessional phase, shown in Fig. 7(b), is seen to be uniform for this mode where the amplitude is large. In contrast, the ***A*** mode map depicted in Fig. 7(c) has regions of large precession along stripes passing through the lattice sites (through the tops of the spherical caps). Here the region of precession overlaps with regions of the sphere where the static configuration does not tip out of plane; this is consistent with the higher resonant

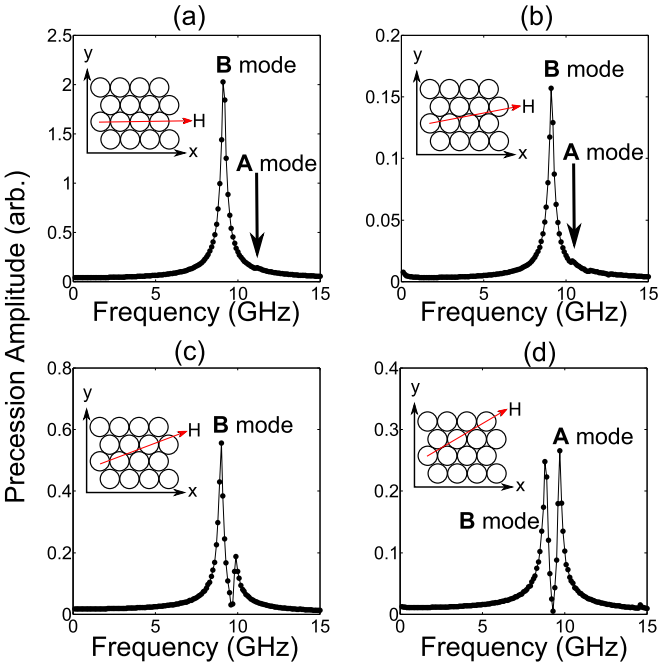

FIG. 6. (Color online) The simulated FMR spectra are shown at 0°, 10°, 20°, and 30° in (a)–(d), respectively. The features that lie close in field-frequency space to the ***A*** and ***B*** modes are denoted. At 0° and 10° the ***A*** mode is weakly excited relative to the ***B*** mode.

frequency. The precessional phase for this running mode is also seen to be uniform [Fig. 7(d)]. Furthermore, a mechanism for amplitude anisotropy and control can be surmised from analysis of the modes in Fig. 7. The ***A***-mode amplitude is dramatically reduced at 0° and 10° where a continuous path that connects the precession amplitudes from sphere to sphere is broken; we believe this is the mechanism responsible for the maxima in the ratio of amplitudes of modes ***B*** and ***A*** described earlier. Figure 8 shows precession and phase maps for the two

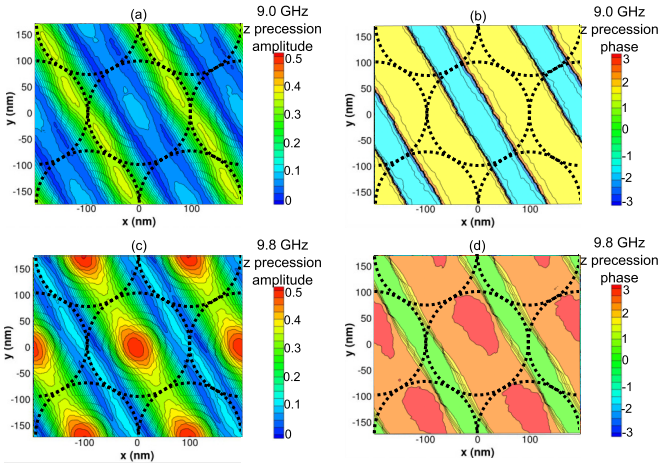

FIG. 7. (Color online) The microscopic details that distinguish the ***A*** mode from the ***B*** mode are best seen when the field is applied at 30°. In (a) and (b) we see the power map and phase map for the ***B*** mode while in (c) and (d) the same information is shown for the ***A*** mode.

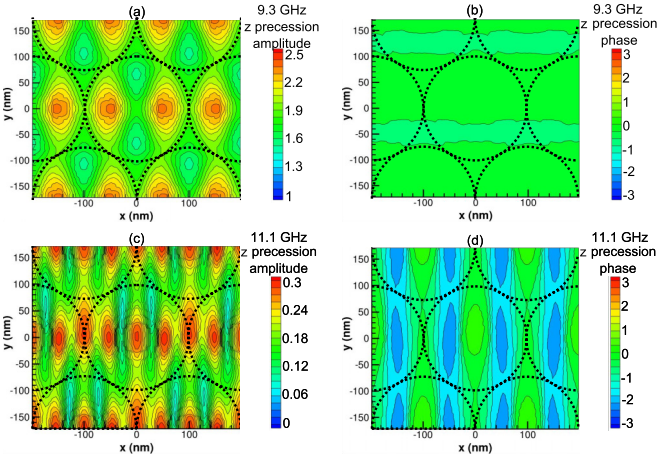

FIG. 8. (Color online) Here we show the ***A*** and ***B*** modes at 0°. (a) and (b) show the amplitude and phase map for the ***B*** mode, which is a type of fundamental Kittel-like mode; (c) and (d) show the amplitude and phase information for the ***A*** mode.

main resonances predicted by simulations when the applied field is at 0°. Figures 8(a) and 8(b) show the ***B***-mode profile, and Figs. 8(c) and 8(d) show the precession and phase maps for the higher-frequency (at fixed field) ***A*** mode. As the field is rotated from 30° to 0°, the lines of maximum amplitude of the ***A*** mode, which connect the tops of the spherical caps at 30°, now connect the top of one cap to the region between two neighboring caps, where the amplitude has broadened into three bands. This higher spatial variation in the magnetization distribution of the mode leads to a blueshift in the frequency and pushes it up to 11.1 GHz.

Before concluding we must point out that the angular dispersion obtained by the numerical simulation is relatively flat for the ***B*** mode, while that of the ***A*** mode exhibits a more pronounced angular variation (Fig. 5). This is in contrast with the experimentally obtained angular dispersions, where that of the ***A*** mode is relatively flat, while that of the ***B*** mode shows more angular variation. We believe that discrepancy originates in defects and imperfections of the colloidal crystal, which is underscored by the apparent lack of sixfold symmetry in the experimental angular dispersions for the modes [Fig. 3(b)]. Nevertheless, we are confident that we have correctly identified the modes based on the following three points of agreement between experimental and numerical results: (1) The ***A*** and ***B*** modes do not cross. (2) The separations in field and frequency space between the modes are in good qualitative agreement. (3) Most importantly, the sudden drop in coupling to the ***A*** mode relative to the ***B*** mode at 0° and ±60° is seen in both experiment and simulation.

In this work we have demonstrated the excitation of multiple $k = 0$ ferromagnetic resonance modes in a thin ferromagnetic film over a large-area nanostructure that has a periodically modulated topography. The presence of multiple Γ-point $k = 0$ modes indicates the existence of a spin-wave band structure. We were able to continuously vary the topography due to an underlying sixfold-symmetric colloidal crystal. Our method of generating ferromagnet resonance modes is an alternative to traditional lithographical means. Experimental

evidence through FMR spectra yields spectra that have a superposition of many modes. Through simulation, we have offered visualizations of the microscopic details that reveal two distinct fundamental modes residing in our system along with higher energy. From an exploratory viewpoint we find that our system underscores both the robustness and fragility of spin-wave modes in nanostructures. Simulations show that the ***A*** mode is highly anisotropic and hence fragile, while the ***B*** mode is considerably more robust. Experimental observations support the details of this conjecture.

The experimental work received support by the Air Force Office of Scientific Research and utilized facilities maintained by the supported Northwestern Materials Research Center supported by the National Science Foundation under Contract No. DMR-1121262; it was equally supported by the National Science Foundation under NSF Award No. EEC-1062784. We would like to thank Varada Bal for her assistance in obtaining AFM images. Work by O.H. was supported by the Department of Energy, Office of Science, Basic Energy Sciences, Division of Materials Science and Engineering. We gratefully acknowledge the computing resources provided on Blues, the high-performance computing cluster operated by the Laboratory Computing Resource Center at Argonne National Laboratory. Any opinions, findings, conclusions, or recommendations expressed in this material are those of the author(s) and do not necessarily reflect those of the National Science Foundation.

[1] V. S. Bhat, J. Sklenar, B. Farmer, J. Woods, J. T. Hastings, S. J. Lee, J. B. Ketterson, and L. E. De Long, Phys. Rev. Lett. **111**, 077201 (2013).

[2] M. Krawczyk and D. Grundler, J. Phys.: Condens. Matter **26**, 123202 (2014).

[3] V. Novosad, F. Y. Fradin, P. E. Roy, K. S. Buchanan, K. Yu. Guslienko, and S. D. Bader, Phys. Rev. B **72**, 024455 (2005).

[4] B. Van Waeyenberge, A. Puzic, H. Stoll, K. W. Chou, T. Tyliszczak, R. Hertel, M. Fähnle, H. Brückl, K. Rott, G. Reiss, I. Neudecker, D. Weiss, C. H. Back, and G. Schütz *et al.*, Nature (London) **444**, 461 (2006).

[5] S. Gliga, A. Kákay, R. Hertel, and O. G. Heinonen, Phys. Rev. Lett. **110**, 117205 (2013).

[6] M. V. Sapozhnikov, S. A. Gusev, B. B. Troitskii, and L. V. Khokhlova, Opt. Lett. **36**, 4197 (2011).

[7] M. V. Sapozhnikov, O. L. Ermolaeva, B. G. Gribkov, I. M. Nefedov, I. R. Karetnikova, S. A. Gusev, V. V. Rogov, B. B. Troitskii, and L. V. Khokhlova, Phys. Rev. B **85**, 054402 (2012).

[8] R. Streubel, D. Makarov, F. Kronast, V. Kravchuk, M. Albrecht, and O. G. Schmidt, Phys. Rev. B **85**, 174429 (2012).

[9] D. Mitin, D. Nissen, P. Schädlich, S. S. P. K. Arekapudi, and M. Albrecht, J. Appl. Phys. **115**, 063906 (2014).

[10] A. Martins, F. Pelegrini, M. M. Soares, and F. Garcia, J. Magn. Magn. Mater. **327**, 44 (2013).

[11] M. Albrecht, G. Hu, I. L. Guhr, T. C. Ulbrich, J. Boneberg, P. Leiderer, and G. Schatz, Nat. Mater. **4**, 203 (2005).

[12] T. C. Ulbrich, D. Makarov, G. Hu, I. L. Guhr, D. Suess, T. Schrefl, and M. Albrecht, Phys. Rev. Lett. **96**, 077202 (2006).

[13] M. Kostylev, A. A. Stashkevich, Y. Roussigné, N. A. Grigoryeva, A. A. Mistonov, D. Menzel, N. A. Sapoletova, K. S. Napolskii, A. A. Eliseev, A. V. Lukashin, S. V. Grigoriev, and S. N. Samarin, Phys. Rev. B **86**, 184431 (2012).

[14] P. Jiang, J. F. Bertone, K. S. Hwang, and V. L. Colvin, Chem. Mater. **11**, 2132 (1999).

[15] C. C. Tsai, J. Choi, S. Cho, S. J. Lee, B. K. Sarma, C. Thompson, O. Chernyashevskyy, I. Nevirkovets, and J. B. Ketterson, Rev. Sci. Instrum. **80**, 023904 (2009).

[16] See Supplemental Material at http://link.aps.org/supplemental/10.1103/PhysRevB.91.134424 for SEM images that show shrinking effects in the colloidal crystal.

[17] D. K. Schreiber, O. G. Heinonen, and A. K. Petford-Long, Phys. Rev. B **80**, 014411 (2009).

[18] J. Sklenar, V. S. Bhat, L. E. DeLong, O. Heinonen, and J. B. Ketterson, Appl. Phys. Lett. **102**, 152412 (2013).

[19] P. K. Muduli, O. G. Heinonen, and J. Åkerman, Phys. Rev. B **83**, 184410 (2011).

[20] K. Rivkin and J. B. Ketterson, J. Magn. Magn. Mater. **306**, 204 (2006).